Numerical Design of a Passive Quadrature Phase and Power Splitter Using 2×2 RI-MMI Couplers with a Fixed Phase Shifter for QPSK and Multicarrier OFDM Applications

Thuy Tran Thi Thanh
EDA LAB, Faculty of Electrical Engineering 1, Posts and Telecommunications Institute of Technology
Hanoi, Vietnam
thuyttt@ptit.edu.vn

Hung Nguyen Tan
Advanced Institute of Science and Technology-The University of Danang
Danang, Vietnam
hung.nguyen@ac.udn.vn

Dung Truong Cao
EDA LAB, Faculty of Electrical Engineering 1, Posts and Telecommunications Institute of Technology
Hanoi, Vietnam
dungtc@ptit.edu.vn

Abstract—We present an optimized design of a 1:4 quadrature phase and power splitter implemented on silicon photonic waveguides. The device operates under the restricted interference regime to achieve a compact footprint. The photonic circuit employs cascaded 2×2 RI-MMI couplers with two spans and a fixed 90-degree phase shifter in one arm, ensuring uniform quadrature phase differences among the output ports. Using 3D-BPM numerical simulations, the optimal MMI length is determined to be 35.4 µm, with a phase shifter length of 26 µm. The simulation results confirm outstanding optical performance, exhibiting low excess loss (<4.6 dB) across a broad spectral range (1500–1600 nm). The device ensures excellent power uniformity across all output ports, with a maximum balance factor of 13 dB, guaranteeing reliable and stable operation. Additionally, the output signals maintain precise 90-degree phase shifts across the four ports (1, 2, 3, and 4), as validated by the signal constellation diagram. These results demonstrate the superior suitability of the proposed device for advanced optical signal processing applications, including QPSK-loaded modulators, multicarrier phase-coded OFDM, optical phasors, and multiphase local oscillators, offering a robust and high-precision solution across multiple wavelength bands.

***Keywords: quadrature phase power splitter, MMI coupler, restricted interference, silicon photonics, optical phasors, QPSK-loaded modulator*.**

I. INTRODUCTION

Currently, photonic integrated circuits are key components in modern and advanced signal processing systems, offering numerous advantages such as ultra-high bandwidth, low loss, compact size, and cost-effectiveness [1]. Additionally, they provide versatile and programmable processing capabilities, making them suitable for a wide range of applications, including optical communication systems [2], high-speed interconnects [3],[4] multiformat modulators [5],[6], optoelectronic devices [7], and photonic neural networks [8],[9]. Among the many photonic circuits, optical power splitters are essential components that enable signal propagation from a single optical transmitter to multiple receivers [10], [11].

In addition to power splitting, an optical power splitter can also perform phase division, generating optical signals with specific phase shifts between the outputs. This capability is crucial in applications that require complicated optical signal processing, such as interferometric phasors [12], non-coherent vector detectors [13], subcarrier orthogonal frequency division multiplexing (OFDM) [13], beamforming optics [14], and Fourier-transform spectrum detectors[15], where precise phase adjustment enhances the sensitivity and reliability of optical transmission. The power splitter ensures that signals at the output ports are not only balanced in power but also synchronized or phase-shifted in a controlled manner, optimizing the overall performance of the optical system. The signal quality, power loss, scalability, and stable phase of the entire system are all directly impacted by the power splitters' performance and design. As a result, creating sophisticated and effective power splitters is essential to the development of data center technology. Besides, silicon-on-insulator (SOI) – based splitters are particularly promising due to their compact design, low optical loss, and CMOS technology compatibility, enabling cost-effective, large-scale photonic integration [1].

Recent developments have focused on optimizing performance metrics such as low insertion loss and consistent power distribution in power and phase splitters. These devices have been engineered using various structural approaches,

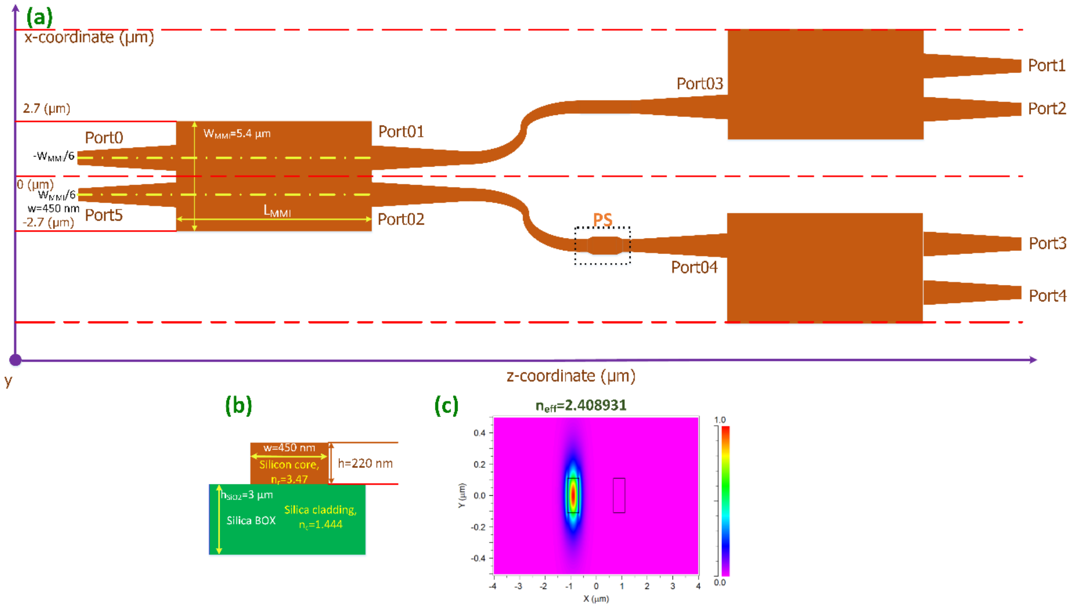

Fig. 1: *The design structure of the proposed device based on a 2×2 MMI in the restricted interference (RI) mechanism using silicon-on-insulator waveguide platform: (a) schematic diagram; (b) cross-sectional view, and (c) computed mode profile of the access waveguide.*

including MMI couplers, Y-junctions, and wave splitters leveraging inverse design techniques. Among these, MMI couplers have stood out for their exceptional stability, seamless integration with silicon photonic platforms, and precise control over both power distribution and phase manipulation.

Multimode Interference (MMI) devices, for instance, have made significant advancements through various design approaches. In [16], silicon-nitride MMI splitters have achieved insertion losses as low as 0.13 dB, making them ideal for data-center applications with stable power distribution. Although silicon nitride (Si_3N_4) is beneficial for reducing back reflection, its integration with existing silicon-based photonic systems remains challenging, potentially affecting scalability and compatibility. Furthermore, the study has focused on the O-band spectrum, which may limit the applicability of the power splitter to other wavelength ranges.

Inverse design techniques, particularly in silicon integrated photonics, have further refined splitters, achieving insertion losses below 0.76 dB and uniformity under 0.84 dB, demonstrating the potential of computational methods in photonic optimization [17]. However, performance may be impacted by manufacturing constraints, such as misalignment during etching and electron scattering during e-beam lithography, which can cause discrepancies between the designed structures and the fabricated devices.

Additionally, Y-branch designs using rectangular waveguides have achieved a power imbalance of just 0.14 dB across the C-band. However, the phase difference between the branched waveguides remains constant, making them unsuitable for phase detection applications [18].

Consequently, almost all previous investigations have only optimized power distribution without considering phase, which limits their applicability in phase-sensitive applications. In this paper, we propose a power splitter structure based on a multimode interferometer using a silicon waveguide with reduced dimensions by utilizing a restricted interference mechanism, with four output ports, where the phase difference between consecutive ports is 90 degrees. This design unlocks numerous potential applications, including orthogonal subcarrier generators, QPSK-loaded modulators, and advanced Fourier-optics signal processing systems. One notable application is its role as an orthogonal subcarrier generator, where the 90° phase shifts at the output ports enable the creation of orthogonal optical carriers. This capability is critical for phase-coded orthogonal frequency-division multiplexing (OFDM) systems and other advanced multi-carrier optical communication technologies. By ensuring orthogonality, the design optimizes spectral efficiency, minimizes inter-channel interference, and enhances transmission performance in high-speed communication networks. Another key application lies in QPSK-loaded modulators, where the precise phase distribution across the four outputs aligns seamlessly with the requirements of QPSK modulation. This integration simplifies system architecture, improves modulation accuracy, and ensures robust signal transmission with reduced noise and distortion. Together, these applications underscore the versatility and efficiency of the proposed design in addressing the growing demands of next-generation optical communication systems. The design is analyzed using the mode propagation method (MPA) and optimized through simulation, with optical performance evaluation conducted using the three-dimensional beam propagation method (3D-BPM).

II. Proposed Design and Geometric Optimization

Fig. 1 describes a principal diagram of a proposed device based on a 2×2 RI-MMI coupler operating under TE polarization. Specifically, Fig. 1(a) shows the side view of the proposed device, Fig. 1(b) shows cross-sectional view of device, and Fig. 1(c) shows the fundamental mode TE0's mode profile for the light input at the single-mode access waveguide (Port0).

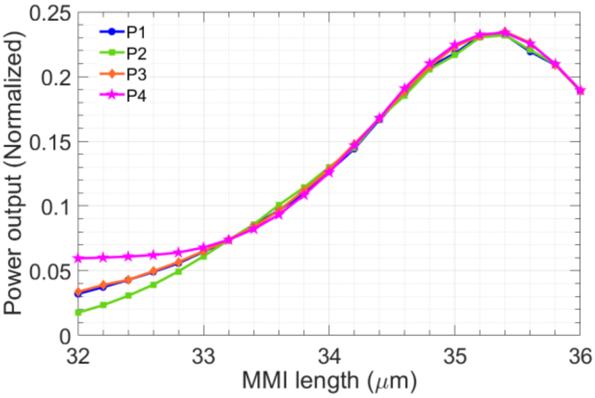

Fig. 2: *Normalized output power dependence on the MMI length swept in the following ranges: from 32 μm to 36 μm.*

The proposed model consists of 2 inputs (Port0 and Port5) and 4 outputs (Port1, Port2, Port3, and Port4), structured from a sophisticated combination of three MMIs with the same width and length, two S-bend waveguides and a Phase Shifter (PS), as shown in Fig. 1(a). Every MMI coupler, at the outset, the width of the 2×2 MMI coupler was initially chosen as W_{MMI} = 5.4 μm. The tapered couplers were designed in the form of an isosceles trapezoid, characterized by their narrower bottom base width of 450 nm, broader top base width of 900 nm, along with a length of 35 μm, have been initially selected. In this configuration, the conventional rectangular access waveguides for coupling to the multimode waveguide were replaced with tapered waveguides to provide input ports and output ports. When switching from single-mode to multimode waveguides, tapered waveguides were selected because they can improve light confinement, lessen the need for exact coupling lengths, and decrease wavelength sensitivity difficulties [20]. The axis of symmetry is defined as the center line of the first multimode interference coupler in the propagation direction. To get high efficiency in the single-mode waveguide regime, the inputs and outputs' thinner bottom bases were connected to an access waveguide with a thickness of 450 nm. Additionally, to interconnect the RI-MMI couplers, S-bend waveguides are employed to prevent optical field overlap. These S-bend waveguides are configured with a length of 200 μm and a gap of 1.5 μm, ensuring efficient signal routing and minimal interference between paths. Besides, a fixed phase shifter (PS) block is placed along the second S-bend waveguide (below S-bend waveguide), with a length of 30 μm and a width of 1.2 μm, to create a 90-degree phase shift relative to the other S-bend.

In Fig. 1(b), the entire device was designed on a silicon-on-insulator (SOI) material platform, with a silicon (Si) guiding layer thickness of h = 220 nm and a 3 μm-thick buried oxide (BOX) layer of silica (SiO_2), sourced from a standard SOI wafer using CMOS semiconductor manufacturing technology. The refractive indices of the silicon core layer and the cladding oxide layer were considered to be constant at n_r=3.47 and n_c=1.444, respectively, in the wavelength range of the third telecom window [21],[22]. In addition, the silicon core layer is surrounded by cladding oxide layers leading to the form of channel waveguides.

The numerical simulation method used was the three-dimensional beam propagation method (3D-BPM), a reliable, accurate, and efficient simulation technique for optical waveguides and photonic structures. This method was implemented to investigate and characterize the guided-wave propagation and optical performance of the proposed device [23]. This study utilized Rsoft's commercial BeamProp-Solution tool employing Yee's cubic mesh, with grid sizes set to $\Delta x = \Delta y = \Delta z$ = 10 nm, ensuring convergence conditions of the Crank-Nicholson algorithm scheme for numerically solving certain partial differential equations, typically hyperbolic PDEs [24].

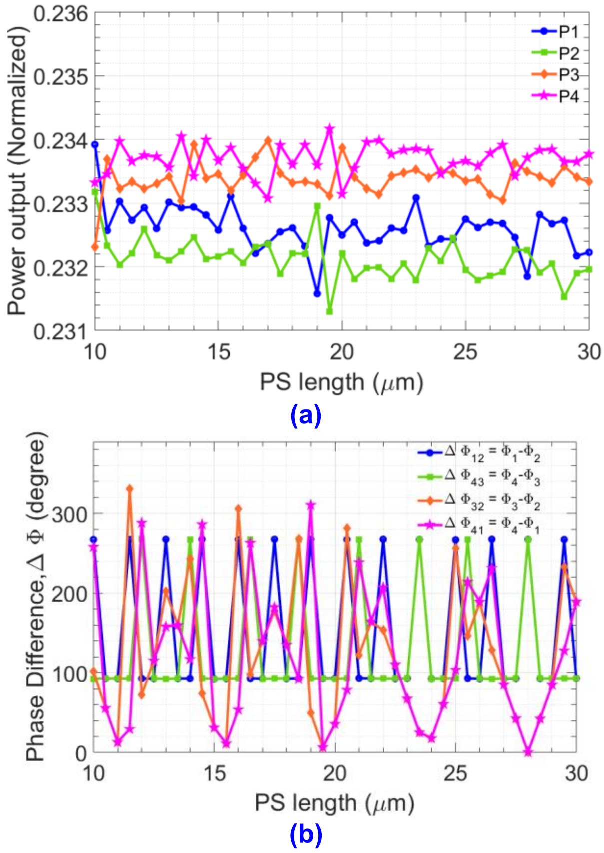

Fig. 3. *(a) Normalized output power transmission characteristic dependence on the PS length is swept in the range from 10 μm to 30 μm, and (b) Phase differences characteristic dependence on the PS length is swept in the range from 10 μm to 30 μm*

In our design, we use two RI-MMI couplers, input and output ports of a RI-MMI are placed at the approximate positions of $y = \pm W_{MMI}/6$ [25], two fold-images are reproduced at a length of $L_{MMI} = (2p+1)L_\pi/2$, with p = 0,1, 2…is a non-negative integer and where L_π the half-beat length of the MMI coupler which is defined by the following formula [25]:

$$L_\pi = \frac{\pi}{\beta_0 - \beta_1} \simeq \frac{4n_r W_e^2}{3\lambda_0} \qquad (1)$$

where β_0, β_1 are corresponding to the propagation constants of the fundamental and first-order modes, respectively; λ_0 = 1550 nm is the operation wavelength in the waveguides; and W_e is the

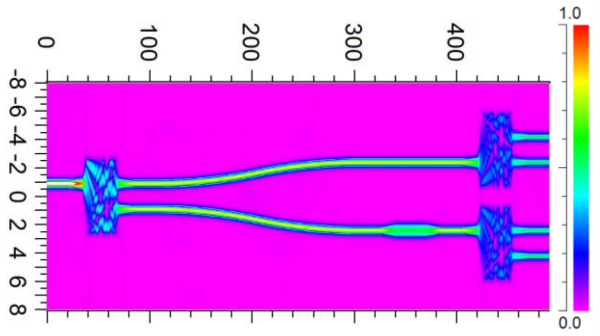

Fig. 4: *3D-BPM simulation of the electric field distribution under TE mode of the designed device at a PS length of 26 µm.*

effective width of the multimode interference coupler which is calculated by the following formula under the TE polarization state:

$$W_e \simeq W_{MMI} + \left(\frac{\lambda_0}{\pi}\right)\left(n_r^2 - n_c^2\right)^{-1/2} \tag{2}$$

Hence, the paired interference regime also exhibits two differently mirrored images at the shortest length of $L_{MMI}=L_\pi/2$.

With configuration parameters of a 2×2 RI-MMI, the effective index, n_{eff}, was approximately 2.59 by using the BPM mode solver, and thus, the numerically calculated values of L_π and $L_\pi/2$ are determined from expressions (1) and (2) corresponding to approximate values of 70.8 µm and 35.4 µm, respectively. In this section, we will examine the optical performances when the MMI couplers length varies in the range around $L_\pi/2$ to find out the valuable length of the proposed MMI couplers so that optical performances are significant. Fig. 2 shows the dependence of the device's output power (P1, P2, P3, and P4) on the length of the three RI-MMI couplers. It is evident that the output power at the four ports is equal when the length of MMI couplers ranges from 33 µm to 36 µm, reaching its maximum value at an MMI couplers length of 35.4 µm.

By applying the multimode interference theory [25], it is well known that in a 2×2 MMI coupler operating in the restricted interference regime, each even mode leads its corresponding odd mode by a phase difference of π/2. This phase difference is determined by subtracting the phase angle of the mirrored output port (Port02) from that of the straightforward output port (Port01) at $z = L_\pi/2$ (referred to as the 3-dB length). At $z = L_\pi$, the phase difference increases to π. Based on this study, when light is input at Port0 of the first MMI, the phase at Port0 is synchronized with Port01 and leads Port02 by 90 degrees. Next, the light from Port01 passes through an S-bend waveguide to reach Port03 (maintaining the phase between these two ports). Meanwhile, the light from Port02 also enters an S-bend waveguide but additionally passes through a PS phase shifter, introducing a 90-degree phase shift, which makes the phase at Port04 lead Port02 by 90 degrees and differ from Port03 by 180 degrees. In the second MMI coupler, the light entering from Port03 is in phase with Port2 and has a 90-degree phase difference from Port1. Similarly, in the third MMI coupler, the light from Port04 is in phase with Port3 and has a 90-degree phase difference from Port4. Thus, the phase at Port3

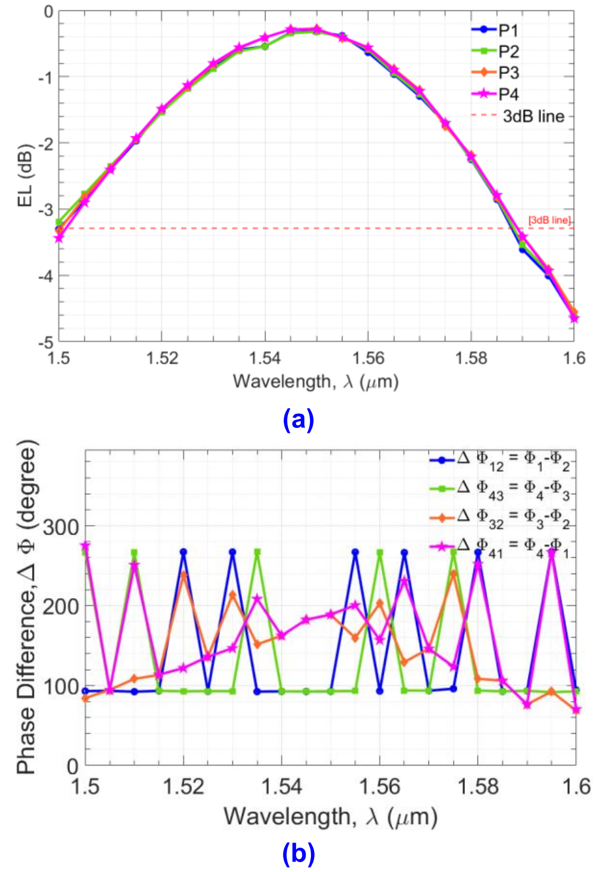

Fig. 5: *Optical performance wavelength-dependency of the designed device in 100-nm spectra for four output ports: (a) excess loss (EL); and (b) phase difference*

differs from Port2 by 180 degrees, and Port4 differs from Port1 by 180 degrees. Furthermore, power splitters for advanced photonic circuit applications, must maintain the phase shift between the four output ports, Port1 to Port2 – $\Delta\Phi_{12}=\Phi_1-\Phi_2$, Port4 to Port3 – $\Delta\Phi_{43}=\Phi_4-\Phi_3$, Port3 to Port2 – $\Delta\Phi_{32}=\Phi_3-\Phi_2$, Port4 to Port1 – $\Delta\Phi_{41}=\Phi_4-\Phi_1$, as a constant, emphasizing minimal fluctuation of the phase difference.

Fig. 3 shows the dependence of the output power and its phase on the length of the PS. It can be clearly seen that when the length of the PS changes from 10 µm to 30 µm, the output power at the 4 ports fluctuates very little, as clearly shown in Fig. 3(a). However, in Fig. 3(b), there is significant oscillation in the phase. Two points of phase difference ($\Delta\Phi_{12} = \Delta\Phi_{43} = 90^o$ and $\Delta\Phi_{32} = \Delta\Phi_{41} = 180^o$) remain stable when the length of the PS (L_{PS}) is 26 µm and 30 µm. To achieve a compact design for the device, we select L_{PS} =26 µm. 3D-BPM simulation of the electric field distribution under TE mode of the designed device at a PS length of 26 µm, is described in Fig. 4.

III. DEVICE PERFORMANCE CHARACTERIZATION

To benchmark the device performances, we also worked out the device excess loss (EL) of the device through each output ports, which can be determined using the formula [26]:

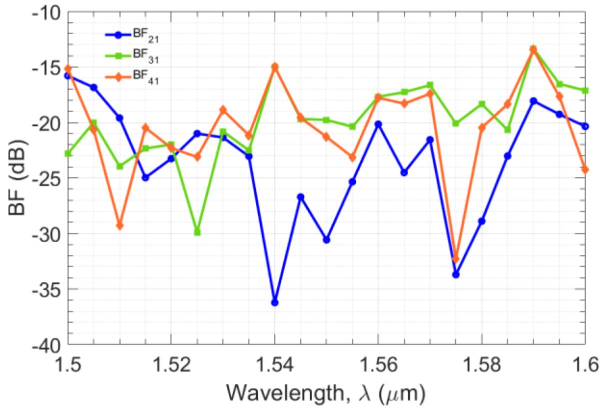

Fig. 6: *Wavelength response balance factor of the proposed power splitter ranging from 1500 nm to 1600 nm*

$$EL = 10\log_{10}\left(\frac{P_{out}}{P_{in}}\right) - 10\log_{10}\left(\frac{1}{4}\right) \quad (3)$$

where P_{out} and P_{in} correspond to the output and input powers, respectively. The constant quantity of $10\log_{10}\left(\frac{1}{4}\right) \approx 6.02$ in Eq. (3) implies that the input light wave is divided into four output ports with a splitting ratio of 1:1:1:1.

Moreover, our device for applications in advanced photonic circuits, such as interferometric phasors, non-coherent vector detectors, and phase modulation circuits, should maintain the phase difference between the four output ports ($\Delta\Phi_{12}=\Phi_1-\Phi_2$, $\Delta\Phi_{43}=\Phi_4-\Phi_3$, $\Delta\Phi_{32}=\Phi_3-\Phi_2$, $\Delta\Phi_{41}=\Phi_4-\Phi_1$) as a constant, emphasizing minimal fluctuation of the phase difference.

As can be seen from Fig. 5(a), the excess losses of the four output ports are consistently similar and closely follow smooth curves versus wavelength response over a broad range of 100 nm from 1500 nm to 1600 nm. However, minimal excess loss is about 0.2 dB at 1550 nm, and 3dB bandwidth is quite large (from 1550 nm to 1585 nm). Besides, the phase differences across wavelengths are illustrated in Figure 5(b). Within the wavelength range of 1540 nm to 1555 nm, the phase deviation remains relatively stable, and the signal pairs maintain their quadrature phase relationship.

Subsequently, we employed standardized equations to ascertain the balance factor of the devices, facilitating the identification of those achieving optimal 1:1:1:1 power splitting. Balance factor is often used to evaluate the performance and uniformity in power distribution or connection between pairs of ports in devices such as splitters or couplers. The balance factor (BF) are described as follows:

$$BF_{i1} = 10\log_{10}\left(\left|\frac{P_{out_i}}{P_{out1}} - 1\right|\right) \quad (4)$$

where P_{outi} are corresponding to the output power of the Port2, Port3 and Port4, respectively. This formula shows the difference or balance of Port2, Port3 and Port4 compared to Port1. Fig. 6 shows the simulation results of the ports balance factor according to the wavelength response from 1500 nm to 1600 nm. The simulation results show that the balance of the four ports due to the limited interference characteristics of the device is very high because, on the decibel scale, BF is small, fluctuating only from the highest value of -13 dB to the lowest value of -36 dB. At the center wavelength of 1550 nm, the balance level is very high because BF = -20 dB (less than 0.2%).

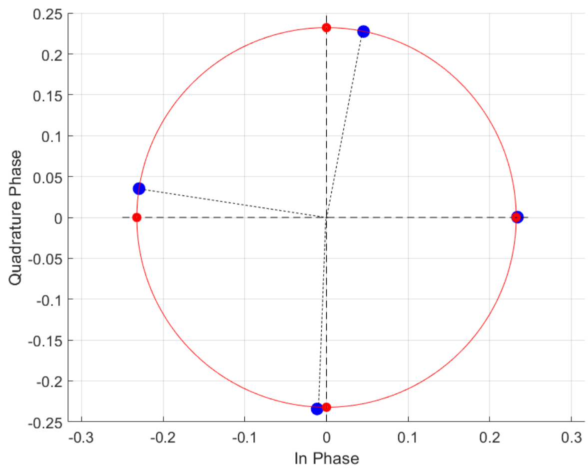

Fig. 7: *Constellation diagram measured at 4 output ports of the device at 1550 nm wavelength*

Finally, another critical parameter for evaluating the performance of the proposed device is the signal constellation, which represents the output power and phase at the four ports, as illustrated in Fig. 7. The figure demonstrates that the output power is nearly equal across all ports, and their phases are approximately quadrature, with a phase deviation from the reference axis ranging between 0.3 and 7 degrees. Therefore, the proposed device is well-suited for applications such as orthogonal subcarrier generators, QPSK-loaded modulators…, as it can generate quadrature-phase signals with balanced power, meeting stringent requirements for performance and phase accuracy. This not only optimizes signal transmission but also ensures high reliability in complex optical signal processing systems.

IV. CONCLUSION

In conclusion, we have utilized an optimized design featuring a silicon 2×2 MMI-based proposed device, employing the restricted interference regime to reduce device length. Numerical simulations conducted using the 3D-BPM method identified the optimal MMI length as 35.4 μm and PS length as 26 μm. Numerical simulation results yielded excellent optical performance for the designed device, with low excess loss (<4.6 dB), including 30 nm of the S-band (1500-1530 nm), the entire C-band (1530 nm - 1565 nm), and 35 nm of the L-band (1565 nm - 1600 nm). Furthermore, the proposed device exhibits excellent power uniformity across all output ports, ensuring a high balance factor critical for reliable operation. Regarding phase, the output signals from ports 1, 2, 3, and 4 demonstrate precise 90-degree phase shifts relative to each other, as illustrated in the signal constellation diagram. These characteristics underscore the device's capability to deliver highly accurate and consistent phase relationships, essential for advanced optical signal processing applications.

REFERENCES

[1] N. Izhaky et al., “Development of CMOS-compatible integrated silicon photonics devices,” IEEE J. Sel. Top. Quantum Electron., vol. 12, no. 6, pp. 1688–1697, 2006, doi: 10.1109/JSTQE.2006.884089.

[2] H. Jia et al., “WDM-compatible multimode optical switching system-on-chip,” Nanophotonics, vol. 8, no. 5, pp. 889–898, 2019, doi: 10.1515/nanoph-2019-0005.

[3] J. Chen, Y. Gong, M. Fiorani, and S. Aleksic, “Optical Interconnects at the Top of the Rack for Energy-Efficient Data Centers,” IEEE Opt. Commun. Mag., vol. 53, no. 8, pp. 141–148, 2015, [Online]. Available: http://www.oejournal.org/J/ArticleQuery/A180509000013

[4] P. Dong, Y. K. Chen, G. H. Duan, and D. T. Neilson, “Silicon photonic devices and integrated circuits,” Nanophotonics, vol. 3, no. 4–5, pp. 215–228, 2014, doi: 10.1515/nanoph-2013-0023.

[5] H. Zhu et al., “Optimized silicon QPSK modulator with 64-Gb/s modulation speed,” IEEE Photonics J., vol. 7, no. 3, 2015, doi: 10.1109/JPHOT.2015.2425875.

[6] J. Witzens, “High-Speed Silicon Photonics Modulators,” Proc. IEEE, vol. 106, no. 12, pp. 2158–2182, 2018, doi: 10.1109/JPROC.2018.2877636.

[7] R. Soref, L. Fellow, and I. Paper, “The Past, Present, and Future of Silicon Photonics,” Sel. Top. Quantum Electron. IEEE J., vol. 12, no. 6, pp. 1678–1687, 2006, doi: 10.1109/jstqe.2006.883151.

[8] R. Stabile, N. Calabretta, and B. Shi, “Large-scale photonic integrated cross-connects for optical communication and computation,” in Optical Fiber Communication Conference (OFC) 2020, 2020, pp. 7–9. doi: 10.1364/OFC-2020-Th3B.1.

[9] J. Jiang, M. Chen, and J. A. Fan, “Deep neural networks for the evaluation and design of photonic devices,” Nat. Rev. Mater., 2020, doi: 10.1038/s41578-020-00260-1.

[10] J. Z. Huang, R. Scarmozzino, and R. M. Osgood, “A new design approach to large input/output-number multimode interference couplers and its application to low-crosstalk WDM routers,” IEEE Photonics Technol. Lett., vol. 10, no. 9, pp. 1292–1294, 1998, doi: 10.1109/68.705620.

[11] and X. Z. Q. A. J. Phillips, J. M. Senior, R. Mercinelli, M. Valvo, P. J. Vetter, C. M. Martin, M. O. van Deventer, P. Vaes, “Redundancy Strategies for a High Splitting Optically Amplified Passive Optical Network,” J. Light. Technol., 2001.

[12] F. Turri, S. Biasi, F. R. Manzano, and L. Pavesi, “A Free-Space Interferometer for Phase-Delay Measurements in Integrated Optical Devices in Degenerate Pump-And-Probe Experiments,” IEEE Trans. Instrum. Meas., vol. 67, no. 12, pp. 2863–2871, 2018, doi: 10.1109/TIM.2018.2830845.

[13] W. Liang et al., “Filterless vector light field photodetector based on photonic-electronic co-designed non-Hermitian silicon nanostructures,” Opt. Express, vol. 33, no. 2, pp. 2395–2405, 2025.

[14] C. Y. Hsu, G. Z. Yiu, and Y. C. Chang, “Free-Space Applications of Silicon Photonics: A Review,” Micromachines, vol. 13, no. 7, 2022, doi: 10.3390/mi13070990.

[15] X. Chen, P. Huang, N. Wang, Y. Zhu, and J. Zhang, “Dual tunable MZIs stationary-wave integrated fourier transform spectrum detection,” Sensors, vol. 21, no. 7, 2021, doi: 10.3390/s21072352.

[16] M. Dror, “An Optical 1×4 Power Splitter Based on Silicon–Nitride MMI Using Strip Waveguide Structures,” 2023, doi: 10.3390/nano13142077.

[17] J. Kim, J. Y. Kim, J. Yoon, H. Yoon, H. H. Park, and H. Kurt, “Experimental demonstration of inverse-designed silicon integrated photonic power splitters,” Nanophotonics, vol. 11, no. 20, pp. 4581–4590, 2022, doi: 10.1515/nanoph-2022-0443.

[18] N. Franata and R. W. Purnamaningsih, “Design of a 1x4 Optical Power Divider Based on Y-Branch Using III-Nitride Semiconductor,” J. Ilm. Tek. Elektro Komput. dan Inform., vol. 8, no. 1, p. 119, 2022, doi: 10.26555/jiteki.v8i1.23646.

[19] Yuzhuang Xie; Haisong Jiang; Kiichi Hamamoto, “1 × 4 Nano-pixel Power Splitter Designed using Overlap-integral Method,” doi: 10.23919/MOC58607.2023.10302858.

[20] Y. Luo, Y. Yu, M. Ye, C. Sun, and X. Zhang, “Integrated dual-mode 3 dB power coupler based on tapered directional coupler,” Sci. Rep., vol. 6, pp. 1–7, 2016, doi: 10.1038/srep23516.

[21] D.-X. Xu et al., “Empirical model for the temperature dependence of silicon refractive index from O to C band based on waveguide measurements,” Opt. Express, vol. 27, no. 19, p. 27229, 2019, doi: 10.1364/oe.27.027229.

[22] S. Dwivedi et al., “Experimental Extraction of Effective Refractive Index and Thermo-Optic Coefficients of Silicon-on-Insulator Waveguides Using Interferometers,” J. Light. Technol., vol. 33, no. 21, pp. 4471–4477, 2015, doi: 10.1109/JLT.2015.2476603.

[23] Y. Jiao, Y. Shi, D. Dai, and S. He, “Accurate and efficient simulation for silicon-nanowire-based multimode interference couplers with a 3D finite-element mode-propagation analysis,” J. Opt. Soc. Am. B, vol. 27, no. 9, p. 1813, 2010, doi: 10.1364/josab.27.001813.

[24] J. Yamauchi, J. Shibayama, O. Saito, O. Uchiyama, and H. Nakano, “Improved finite-difference beam-propagation method based on the generalized Douglas scheme and its application to semivectorial analysis,” J. Light. Technol., vol. 14, no. 10, pp. 2401–2406, 1996, doi: 10.1109/50.541236.

[25] L. B. Soldano and E. C. M. Pennings, “Optical Multi-Mode Interference Devices Based on Self-Imaging: Principles and Applications,” J. Light. Technol., vol. 13, no. 4, pp. 615–627, 1995, doi: 10.1109/50.372474.

[26] Q. Yi et al., “Silicon MMI-based power splitter for multi-band operation at the 1.55 and 2 μm wave bands,” Opt. Lett., vol. 48, no. 5, p. 1335, 2023, doi: 10.1364/ol.486428.